# Aligned Epitaxial SnO$_2$ Nanowires on Sapphire: Growth and Device Applications

Xiaoli Wang,[†,∥] Noppadol Aroonyadet,[†,∥] Yuzheng Zhang,[§] Matthew Mecklenburg,[∥] Xin Fang,[§] Haitian Chen,[†] Edward Goo,[§] and Chongwu Zhou*[,†]

[†]Department of Electrical Engineering, [§]Department of Chemical Engineering and Material Science, and [∥]Center for Electron Microscopy and Microanalysis, University of Southern California, Los Angeles, California 90089, United States

S Supporting Information

ABSTRACT: Semiconducting SnO$_2$ nanowires have been used to demonstrate high-quality field-effect transistors, optically transparent devices, photodetectors, and gas sensors. However, controllable assembly of rutile SnO$_2$ nanowires is necessary for scalable and practical device applications. Here, we demonstrate aligned, planar SnO$_2$ nanowires grown on A-plane, M-plane, and R-plane sapphire substrates. These parallel nanowires can reach 100 μm in length with sufficient density to be patterned photolithographically for field-effect transistors and sensor devices. As proof-of-concept, we show that transistors made this way can achieve on/off current ratios on the order of 10^6, mobilities around 71.68 cm^2/V·s, and sufficiently high currents to drive external organic light-emitting diode displays. Furthermore, the aligned SnO$_2$ nanowire devices are shown to be photosensitive to UV light with the capability to distinguish between 254 and 365 nm wavelengths. Their alignment is advantageous for polarized UV light detection; we have measured a polarization ratio of photoconductance (σ) of 0.3. Lastly, we show that the nanowires can detect NO$_2$ at a concentration of 0.2 ppb, making them a scalable, ultrasensitive gas sensing technology. Aligned SnO$_2$ nanowires offer a straightforward method to fabricate scalable SnO$_2$ nanodevices for a variety of future electronic applications.
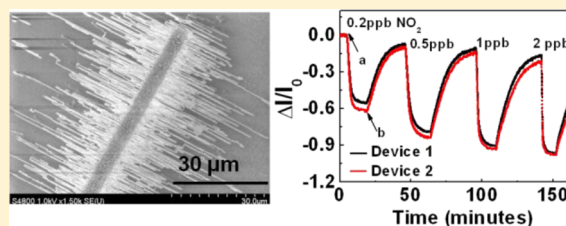
KEYWORDS: Nanowire, tin oxide, epitaxy, guided growth

Research on aligned semiconducting nanowires has gained significant momentum in recent years due to their importance in building scalable and dimensionally controllable bottom-up devices for various applications, ranging from diodes and transistors to chemical and biological sensors. Many methods have been developed to manipulate these nanowires postgrowth, including the Langmuir−Blodgett compression,[1−3] pattern transfer,[4] mechanical shear,[5] fluid flow in microchannels,[6] and orientation by an electric field.[7] With a recently reported nanocombing method, misalignment of nanowires can be controlled within ±1° with small cross defect density of 0.04 nanowires per μm.[8] On the other hand, guiding the direction of nanowire growth by using the epitaxial relation between the nanowire and the substrate combines synthesis and assembly into one single step. This also provides control of nanowire crystallographic orientation and direct fabrication of nanowire devices on growth substrates without the need for a transfer process. Substrate guided growth of semiconducting nanowires has been successfully demonstrated for GaN nanowires on sapphire,[9] ZnO nanowires on sapphire,[10,11] InAs nanowires on InAs,[12] and InP nanowires on InP.[13] In this work, we show that synthesized SnO$_2$ nanowires not only demonstrate guided growth on R-plane and annealed A- and M-plane sapphire but also provide good assembly for easy integration in various electronic applications.

The n-type semiconductor SnO$_2$ is a direct, wide bandgap (3.6 eV)[14] material with high electrical conductivity, optical transparency, and sensitivity to adsorbed molecules. Successful applications of SnO$_2$ for field-effect transistors,[15,16] transparent devices,[17] and gas sensors[18−21] have already been realized. SnO$_2$ nanowires can be especially advantageous for these applications reliant on their dimensional compatibility with nanoelectronics and their high surface to volume ratio that is important for sensitivity. Here we show that aligned, planar SnO$_2$ nanowires can be used to achieve better control of the transistor channel orientation, which creates an advantage for various sensing applications. In addition, SnO$_2$ nanowires have a rutile structure not exhibited in nanostructures in previous substrate guided growth studies, and their synthesis deserves further investigation.

We chose sapphire as the growth substrates for the aligned SnO$_2$ nanowires because of its widely demonstrated ability to guide nanowire[9−11] and nanotube[22,23] growth. We first investigated the effect of annealing A (11$\bar{2}$0), M (10$\bar{1}$0), and R (1$\bar{1}$02) plane sapphire on optimizing the growth conditions for the rutile structured SnO$_2$ nanowires. The orientations for each of the three sapphire planes are shown in Figure 1a−c
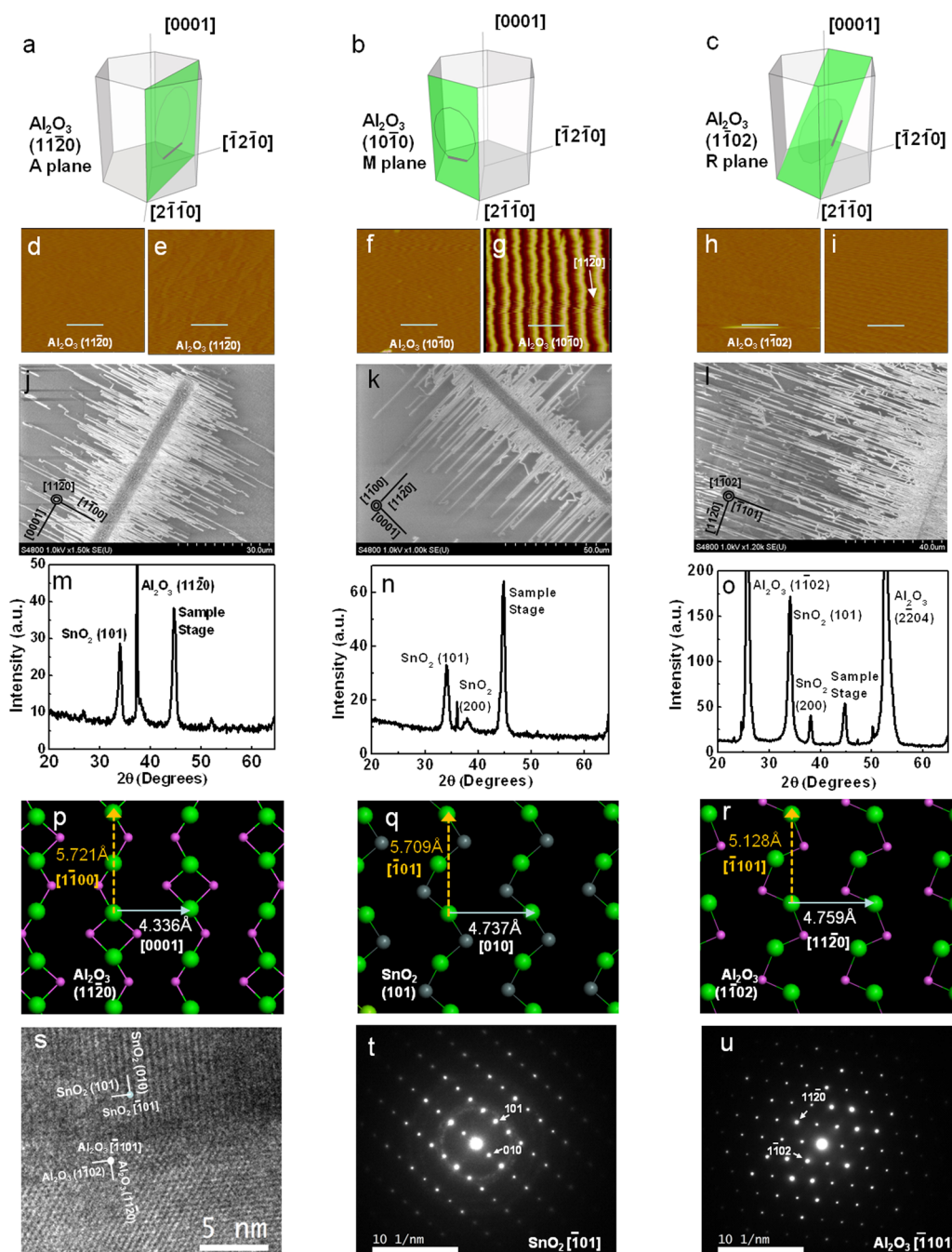
Figure 1. Aligned SnO$_2$ nanowire growth study. (a−c) Orientation of A-plane (a), M-plane (b), and R-plane (c) sapphire. Wafers are outlined on each plane with the wafer flat bolded. (d−i) AFM scans of A (d−e), M (f,g), and R (h,i) sapphire surfaces before (d,f,h) and after (e,g,i) annealing. Scale bars are 30 nm. (j−l) SEM images of aligned SnO$_2$ nanowires grown on A-plane (j), M-plane (k), and R-plane (l) sapphires. Sapphire orientations are included on the bottom left. (m−o) XRD data for aligned SnO$_2$ nanowires grown on A-plane (m), M-plane (n), and R-plane (o) sapphires show all three planes tend to interface the SnO$_2$ (101) plane. (p−r) Diagrams of atomic arrangement for A-plane sapphire (p), (101) plane SnO$_2$ (q), and R-plane sapphire (r). Dashed vectors show sapphire to SnO$_2$ lattice alignment in the y-direction while solid vectors show alignment in the x-direction. Green circles are oxygen atoms, pink circles are aluminum atoms, and gray circles are tin atoms. (s) TEM image of a cross-sectional view of aligned SnO$_2$ nanowire on sapphire. (t) Electron diffraction pattern of SnO$_2$ nanowire taken from similar cross-section locations. (u) Electron diffraction pattern of cross-section of R-plane sapphire.

along with the orientation of the wafer flat, which is indicated as the bold edge of the outlined wafer in each plane. High-temperature annealing of each sapphire plane was done in ambient air, and atomic force microscopy (AFM) images were examined before and after annealing. Pristine substrates of A plane (Figure 1d), M plane (Figure 1f), and R plane (Figure 1h) all show planar surfaces. After annealing, however, we

observed clear V-shaped nanogroove structures in the M-plane sapphire that are approximately 15 nm deep, shown as Figure 1g. The presence of the grooves is consistent with observations that were used to explain the mechanism of graphoepitaxial growth of aligned ZnO and GaN nanowire,[9,11] and the same mechanism can be applied to parallel SnO$_2$ nanowires on annealed M plane as well. It is because the M-plane sapphire is

thermodynamically unstable during high-temperature annealing. Its crystal facet will be transformed from $(10\bar{1}0)$ to nanostructure grooves composed of S-plane and R-plane facets along $[11\bar{2}1]$ direction.[11] On the other hand, A- and R-plane sapphire retained their planar surface structure after annealing, as can be seen in Figure 1e,i, respectively. The lack of surface features on the A-plane and R-plane sapphire suggests that the alignment of SnO_2 nanowires on these planes are aligned by lattice guided growth instead, which is in agreement with the mechanism of aligned ZnO growth.[11]

Before synthesis, catalysts were first deposited onto both annealed and nonannealed sapphire substrates in the shape of Au stripes using standard photolithography and electron beam evaporation. The guided SnO_2 nanowires were grown using a vapor−liquid−solid (VLS) process in a low pressure chemical vapor deposition (CVD) system. Details of the synthesis can be found in the Supporting Information. After synthesis, aligned SnO_2 nanowire growth was confirmed and characterized by scanning electron microscopy (SEM) imaging. We first observed that substrate annealing affected SnO_2 nanowire growth differently, depending on the plane orientation of the sapphire substrate. On unannealed M-plane sapphire, SnO_2 nanowires grew in two perpendicular directions, crossing each other such that the length between each junction is under 5 μm. Parallel SnO_2 nanowires on the M plane were observed only on annealed M planes. SnO_2 nanowires grown on unannealed A-plane sapphire had short lengths under a few micrometers and poor parallel alignment. On R-plane sapphires, however, no significant difference between SnO_2 nanowire growth on annealed and on unannealed substrates were found. Therefore, the following experiments and discussions were carried out with aligned SnO_2 nanowires grown on annealed A-plane, annealed M-plane, and unannealed R-plane sapphires. We have quantitatively and statistically analyzed crucial nanowire assembly parameters from SEM images of SnO_2 nanowires taken from 20 samples of these 3 types of sapphire substrates, and the results are shown in Figure S1 in the Supporting Information. From histograms of nanowire density, alignment defect density (defined as crossing or crooked nanowires), and misalignment angle of SnO_2 nanowires on three different types of substrates in Supporting Information Figure S1, SnO_2 nanowires synthesized on unannealed R-plane sapphire substrates showed high density (4.11 ± 0.11 nanowires/μm), low-alignment defect density (0.35 ± 0.34 nanowires/μm), and good alignment (98% within $\pm1°$ misalignment). Densities of aligned SnO_2 nanowires on annealed A-plane and annealed M-plane sapphire are 2.79 ± 0.75 and 1.32 ± 0.46 nanowires/μm, respectively, lower than the density on R-plane sapphire. Even though nanowires on annealed A-plane sapphire showed higher alignment defect density (1.38 ± 0.65 nanowires/μm) than nanowires on annealed M-plane sapphire (0.53 ± 0.26 nanowires/μm), they have comparable distribution of alignment angles (91% of nanowires on A plane and 90% of nanowires on M plane are within $\pm1°$).

On the annealed A-plane sapphire, SnO_2 nanowires grew parallel to the $[1\bar{1}00]$ direction or perpendicular to the direction of nanowires grown the annealed M-plane sapphire shown in Figure 1j. Conversely, Figure 1k shows that SnO_2 nanowires aligned on the annealed M-plane sapphire grew parallel to the $[11\bar{2}0]$ direction, which is perpendicular to the A plane. Figure 1l shows SnO_2 nanowires synthesized on the R-plane sapphire with a clear alignment in the $[\bar{1}101]$ direction.

The SEM images show the nanowire lengths on all planes range from 10 to 100 μm with a large percentage of wires between 50 and 100 μm in length. The long nanowires allow for simple patterning of source, drain, and gate electrodes using standard photolithography techniques. Further characterization using SEM and AFM revealed that the average diameters of wires on all planes to be between 50 to 75 nm.

X-ray diffraction (XRD) patterns of the nanowires were taken to investigate the relationship between the rutile structured SnO_2 nanowires and the sapphire substrates. Figure 1m−o shows the SnO_2 nanowire orientation on the A-plane, M-plane, and R-plane substrates, respectively. The SnO_2 (101) peak appears as the dominant SnO_2 peak on all three sapphire planes, suggesting SnO_2 (101) to be the interfacing plane in all three cases. Minor peaks such as SnO_2 (200) may be caused by random, unaligned SnO_2 nanowires grown around the catalyst stripe. Confirmation of A-plane and R-plane sapphire substrates is evident in the Al_2O_3 $(11\bar{2}0)$, $(1\bar{1}02)$, and $(2\bar{2}04)$ peaks that appear in the corresponding XRD plots. Although no M-plane peak is seen, it can be explained by the irregular surface caused by the grooves found after annealing.

The preference of interfacing the SnO_2 (101) plane with sapphire is supported by several previous reports[24−26] from which the relative orientation between the aligned SnO_2 nanowires and the sapphire planes can also be predicted. For example, the interface between tilted SnO_2 nanowires and A-plane sapphire was reported as SnO_2 (101) $[\bar{1}01]$‖$Al_2O_3(11\bar{2}0)$ $[1\bar{1}00]$[24] and is assumed to be the orientation between our aligned SnO_2 nanowires and the A-plane sapphire substrate as well. This is illustrated in Figure 1p,q, which respectively depict the atomic structure of the Al_2O_3 $(11\bar{2}0)$ and SnO_2 (101) plane. The interface of the two planes overlapped in such a way that the dashed axis in Figure 1p aligns with the dashed axis in Figure 1q, while the solid axis aligns with the corresponding solid axis. Because the nanowires grow epitaxially along Al_2O_3 $[1\bar{1}00]$, it follows that the SnO_2 nanowire growth direction on A-plane sapphire is SnO_2 $[\bar{1}01]$.

Additionally, the (101) surface of SnO_2 films have been observed to interface R-plane sapphire[25,26] with the two materials orientated such that SnO_2(101) $[010]$‖$Al_2O_3(1\bar{1}02)$ $[11\bar{2}0]$. This also agrees with the orientation for our aligned SnO_2 nanowires on R-plane sapphire, and it is illustrated through the atomic arrangements of the SnO_2 (101) and Al_2O_3 $(1\bar{1}02)$ surfaces shown in Figure 1q,r, respectively. The aligning axes are drawn with the same line type again. Because the SEM image in Figure 1l revealed that nanowires grow along the Al_2O_3 $[1\bar{1}01]$ direction on R-plane sapphire, we can conclude that the SnO_2 nanowires on the R plane also grow along the SnO_2 $[\bar{1}01]$ direction. On the other hand, nanowires on the annealed M-plane sapphire are aligned along the nanogrooves in which the exposed surface is mainly R plane.[11] Thus, the interface relationship on annealed M-plane sapphire is also SnO_2 (101) $[010]$‖Al_2O_3 $(1\bar{1}02)$ $[11\bar{2}0]$. However, because the nanogrooves are oriented in the Al_2O_3 $[11\bar{2}0]$ direction, the nanowire growth direction on annealed M plane becomes SnO_2 $[010]$.

The aligned SnO_2 nanowire orientation on R-plane sapphire was further confirmed using transmission electron microscopy (TEM) imaging of a cross-sectional sample prepared by JEOL 4500 focused ion beam (FIB). The schematic in Figure S2a in the Supporting Information illustrates that the cross-section was cut perpendicularly to the nanowire growth direction, and the direction of the electron beam from the JEOL 2100F TEM
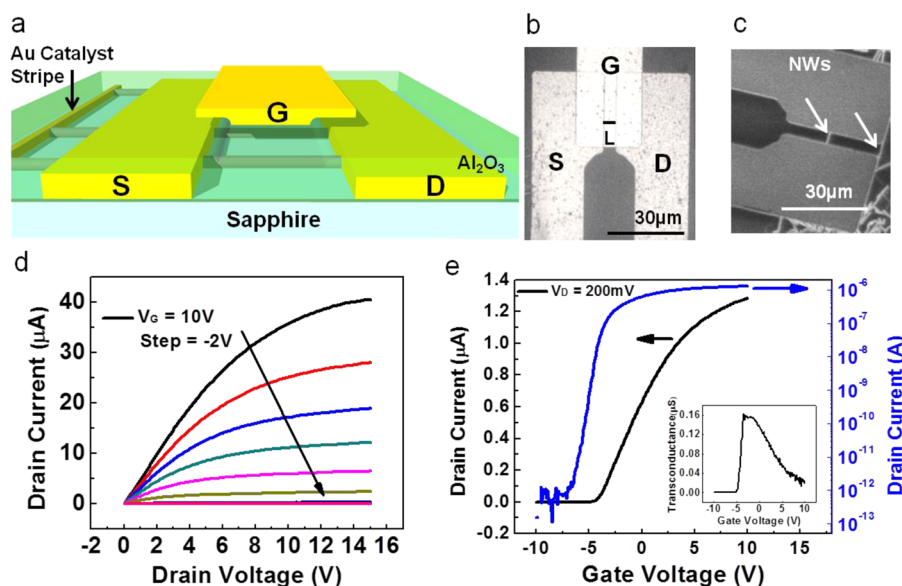
Figure 2. Aligned SnO_2 nanowire transistor study. (a) Diagram of device fabrication. (b) Top-view optical image of an aligned SnO_2 nanowire transistor. (c) SEM image of two aligned SnO_2 nanowires bridging the source and drain electrodes of a nanowire transistor. (d) I_D–V_D family plot of the transistor shown in (c). (e) I_D–V_G plot of the transistor in (c) plotted with standard scale in black and logarithmic scale in blue. The subplot shows the transconductance of the same device.

is parallel to the nanowire growth. The resulting TEM image can be seen in Figure 1s. The growth direction of the nanowire can be confirmed to be SnO_2 $[\bar{1}01]$ from the diffraction pattern of Figure 1t, where two normal planes are indicated to be SnO_2 (101) and SnO_2 (010). Similarly, we can confirm that the nanowires grow along the sapphire $[1\bar{1}01]$ direction from Figure 1u, where the two normal planes are Al_2O_3 $(1\bar{1}02)$ and Al_2O_3 $(11\bar{2}0)$. The indexing of the diffraction spots is confirmed using CrystalMaker simulations for diffraction into the sapphire $[\bar{1}101]$ axis and the SnO_2 $[\bar{1}01]$ axis, which are overlaid in Supporting Information Figure S2b,c, respectively. The exact locations from the cross-section used to obtain the diffraction patterns for the sapphire and SnO_2 nanowire are shown in Supporting Information Figure S2d. The orientations and interface planes from TEM analysis show agreement with the XRD data and orientation data from literature. Figure S3a in the Supporting Information shows a high-resolution TEM image of an aligned SnO_2 nanowire taken from the same spot as Figure 1s. Lattice spacing of SnO_2 along $[010]$ direction and Al_2O_3 in $[11\bar{2}0]$ are measured to be approximately 4.8 Å, which is close to values specified in Figure 1q,r. Supporting Information Figure S3b shows a high-resolution SEM image of a single aligned SnO_2 nanowire on an R-plane sapphire substrate with smooth surface and width about 123 nm.

We also observed that synthesis pressure significantly affected whether the resultant nanowires are parallel, planar SnO_2 nanowires, or randomly oriented, free-standing nanowires. By increasing the pressure inside the furnace to atmospheric pressure during the synthesis, we obtained a higher density of SnO_2 nanowires on top of the Au catalyst. Supporting Information Figure S3c shows an SEM image of SnO_2 nanowires grown on R-plane sapphire under such an atmospheric condition. The densely interlaced nanowires appear similar to freestanding nanowire forests grown on Si substrates.[16] They are connected to the substrates only at one end and are not epitaxially in-plane with the sapphire surface. Careful sonication of this dense SnO_2 nanowire forest revealed no significant layers of aligned SnO_2 nanowire underneath. The

possibility of a hidden layer of aligned nanowires being removed during the sonication is ruled out because purposeful sonication of visibly aligned SnO_2 nanowires under the same conditions was unsuccessful. This comparison suggests that synthesis at atmospheric pressure, where the Sn vapor partial pressure is large, favors growth of dense nanowires that are forestlike and unaligned, while lower Sn partial pressure allows the nanowires to grow in alignment on the substrate surface. Similar effect of partial pressure on nanowire growth was also observed for InAs nanowires,[12] where the Gibbs−Thomson equation was used to show that higher precursor vapor pressure is required for free-standing nanowires than that required for planar nanowires.

Scalable device fabrication is an important step for practical integration of metal oxide nanowires in applications like display and memory technology[15,27] and various types of sensors.[28,29] After synthesis, aligned SnO_2 nanowires grown on sapphire were fabricated as field effect transistors (FETs) using standard photolithography technology. Details of the fabrication are described in the Methods Section in the Supporting Information. The finished device is represented in the schematic in Figure 2a, which shows how the electrodes can be easily patterned perpendicular to the length of the SnO_2 nanowire without complex techniques such as electron beam lithography. A top-view optical image of one device is shown in Figure 2b, and the alignment of SnO_2 nanowires across the source and drain electrodes can be seen in the SEM image of Figure 2c, where two nanowires that grew parallel to each other are covered with metal electrodes oriented perpendicularly to the length of nanowires. The FET characteristics of this device with the two parallel nanowires are shown in Figure 2d,e. In the drain current (I_D) versus the drain-to-source voltage (V_D) plot of Figure 2d, the device exemplifies a MOSFET behavior in which the I_D is linearly dependent on V_D at low drain voltages but saturates when V_D increases beyond a few volts. The current is also shown to increase with the gate voltage (V_G). At a V_G of 10 V, the current can reach 40 μA, while at a V_G of −4 V the current is shown to be turned off. The I_D versus V_G plot
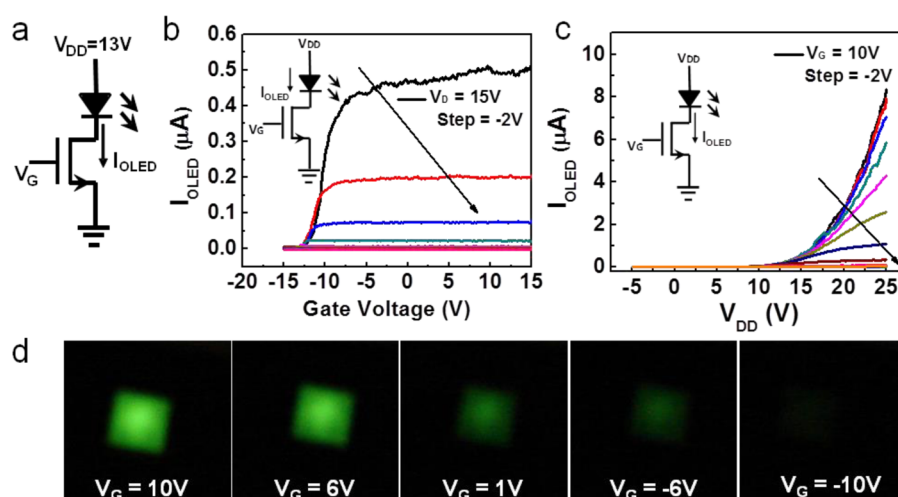
Figure 3. Aligned SnO$_2$ nanowire FET control circuit for OLED. (a) Circuit diagram of OLED connection to FET. (b) I_{OLED}−V_G family curve. (c) I_{OLED}−V_{DD} family curve. (d) Optical images of OLED intensity as V_G decreases.

in Figure 2e also confirms that the current is turned off with V_G < −4 V. The curve is measured at V_D = 200 mV, where the transistor is in the ohmic region. The plot of I_D in log scale indicates a good on/off ratio of over 10^6, and the subplot shows the transconductance (dI_D/dV_G) of the device to be around 0.16 μS. This transconductance value and the relationship $dI_D/dV_G = \mu(C/L^2)V_D$ can be used to calculate the electron mobility, μ. The nanowire channel length (L) is 5 μm. The gate capacitance (C) can be estimated by modeling the nanowires as cylinders on the sapphire plane.[15] Assuming that the aluminum oxide dielectric constant is around 9[30] and using an average nanowire diameter of 75 nm each, the gate capacitance is calculated to be 1.79 × 10^{-15} F for each nanowire.[15,31−33] From these values, the corresponding electron mobility is 55 cm^2/V·s. To benchmark its device performance, we note that the aligned SnO$_2$ nanowire device has an on/off ratio and mobility that is higher than that of devices based on individual spin-coated SnO$_2$ nanowires previously demonstrated using a laser ablation technology.[16] This confirms the high quality of our aligned SnO$_2$ nanowires and supports the idea that aligned nanowire transistors have the potential to be fabricated with superior yield and scalability compared to individual nanowire device and are expected to have superior performance compared to nanowire network devices.

To show the performance that the aligned SnO$_2$ nanowire transistors can produce, we have plotted histograms of device performance from 20 devices in the Supporting Information. Figure S4a shows that the I_D measured at V_D = 200 mV and V_G = 10 V are typically between 1 and 3 μA with the average I_D being 1.48 μA and the standard deviation being 0.33 μA. The on/off current ratios (Supporting Information Figure S4b) for all the transistors fall in the range of 10^4 to 10^8 with majority (13 out of 20 devices) showing on/off ratios of 10^5 to 10^6. In Supporting Information Figure S4c, the average transconductance of the 20 devices is 157 nS with a standard deviation of 37.23 nS. The threshold voltage (V_{TH}) variation is shown in Supporting Information Figure S4d, where the average V_{TH} is −4.22 V with a standard deviation of 0.81 V. The histogram of electron mobility is shown in Supporting Information Figure S4e with an average of 71.68 cm^2/V·s.

The high I_{on}, on/off ratio and mobility of the aligned SnO$_2$ nanowire transistor are highly desired traits in many micro- and

nanoelectronic applications such as organic light-emitting diode (OLED) control circuitry. OLEDs are a promising display technology due to many of their superior characteristics such as lightweight, excellent color purity, low-power consumption, and so forth.[34,35] To fully develop OLED as a low-cost, large-scale product, much research is currently ongoing to study the material and fabrication of the OLED and its driving circuit. Aligned SnO$_2$ nanowire transistors are compatible with flexible and transparent electronics in addition to having good electronic properties as mentioned above and can be a good candidate for the driving circuit. As a proof of concept, we demonstrate the application of a top-gated, aligned SnO$_2$ nanowire FET as the control for an external OLED with the structure of 4,4′-bis[N-(1-naphthyl)-N-phenylamino]biphenyl-(NPD)/tris(8-hydroxyquinoline) aluminum (Alq3). This is a green light OLED with indium tin oxide (ITO) as the anode and aluminum (Al) as the cathode. The entire circuit is connected as shown in Figure 3a. A coaxial cable with a clamp terminal is connected to V_{DD} on one side while its clamp side is placed on the cathode of the OLED. Another cable of the same type has its clamp side placed on the anode of the OLED while the other side is connected to the drain of the aligned SnO$_2$ nanowire FET. The relationship between the current through the diode (I_{OLED}) and the power supply (V_{DD}) is plotted in Figure 3b, and the curves show good diode behavior with a clear-cutoff region and triode region under different SnO$_2$ nanowire FET gate voltage (V_G), showing good control from the FET over the OLED. The cutoff voltage of V_{DD} is around −13 V in accordance with the threshold voltage of the OLED. From the I_{OLED}−V_G curves in Figure 3c, the FET is capable of providing enough driving current for the OLED, which requires approximately 0.2 μA to have observable light emission. The optical images in Figure 3d show the OLED at various light intensities under different V_G values of the SnO$_2$ nanowire FET at fixed V_{DD} = 13 V. From the optical images, the OLED is very bright when V_G = 10 V, gets dimmer as V_G decreases toward negative voltages, and is totally turned off when V_G becomes more negative than −10 V, corresponding to the I_{OLED}−V_G curve measured at V_{DD} = 13 V in Figure 3b, where the curve enters the cutoff region around −10 V.

SnO$_2$ has also been documented to have excellent photo-conductive properties, whether as a thin film[14] or as a
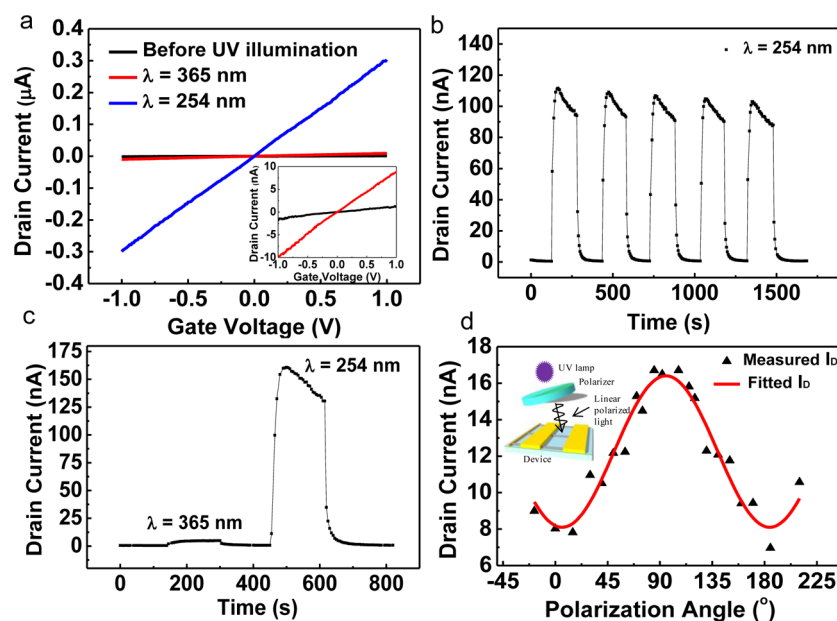
Figure 4. Photoconduction and polarization detection. (a) $I_D–V_D$ curves of aligned SnO_2 device before UV illumination (black), after 365 nm UV illumination (red), and after 254 nm UV illumination (blue). Expanded curves for before and 365 nm illumination are presented in the subplot for clarity with the same color legend. (b) Real-time detection of 254 nm UV illumination on an aligned SnO_2 device as the UV lamp is turned on and off for five cycles. (c) Real-time detection of 2 different wavelengths using one aligned SnO_2 device. (d) Polarized 254 nm UV detection. Black triangles are averaged peak I_D during the time that the UV lamp is turned on at the corresponding angle. The red curve is fitted data showing $\cos 2\theta$ dependence.

nanowire,[16] and we expect that the alignment of SnO_2 nanowires will further improve this response. The parallel alignment of the nanowires is expected to be especially advantageous for having strong sensitivity to polarized light due to the uniformity of the nanowire orientation between the source and drain electrodes of the FET device. To test the photoconductive properties of the devices, two UV lamps with wavelength of 254 and 365 nm, placed 2 cm above our aligned SnO_2 nanowire FET, were used as photo source. No gate voltage was applied to the nanowire FET, and measurements were taken in air, at room temperature, and under indoor incandescent light. From the $I_D–V_D$ data presented in Figure 4a, enhanced conduction was observed for UV illumination of both wavelengths. However, the 254 nm light induced a significantly larger magnitude of response than that elicited from the 365 nm light, whose expanded curve is shown in the subplot. The zero-bias conductance before and after the 365 nm UV light exposure is calculated to be 1.1 and 8.8 nS, respectively, and the illumination with 254 nm UV light induced a conductance value of 320 nS. This on/off ratio is comparable to those reported for GaN nanowire FET photoconduction.[36] The mechanisms of photoconduction in metal oxides and the difference in conduction due to the two wavelengths are well documented.[16,37] Because SnO_2 has a 3.6 eV bandgap, a photon from the 254 nm UV light with an energy of 4.9 eV can sufficiently excite electron–hole pair generation while a photon from the 365 nm light with an energy of 3.4 eV cannot. However, a small increase in conduction in response to the 365 nm light still occurs due to the nonzero photon energy spectrum. The second photoconduction mechanism occurs because UV light cleanses adsorbed species from the nanowire surface and frees electrons from reduced molecules such as O_2^-. Real time UV detection was also performed by turning the 254 nm UV lamp on and off for five cycles, as shown in Figure 4b. In this experiment, the V_D

of the device was fixed at 500 mV. The conductance of the nanowire showed a rapid increase from 1.3 nS to an averaged on-conduction of 193 nS upon exposure to UV light. Detailed data analysis revealed that the conductance of the nanowire increased to about 50% of its average on-current within 5 s after the UV lamp was turned on and reached about 90% within 10 s. The aligned SnO_2 nanowire sensor also exhibited a high recovery speed, as seen in the sharp current drop when the light was turned off. The real-time current response to the 365 nm UV illumination is shown in Figure 4c as a comparison to the 254 nm light. The difference in response reiterates the ability of the nanowire device to distinguish specific wavelengths, and the FET shows good stability when detecting multiple light sources. Moreover, the stability of photocurrent has been investigated on the same photodetector as shown in Figure S5 in the Supporting Information. The aligned SnO_2 nanowire detector was illuminated using the 254 nm UV lamp over 100 min shown in Supporting Information Figure S5a. The photocurrent exhibited a sharp response similar to the result shown in Figure 4b upon UV illumination and reached its steady state after 50 min as shown in Supporting Information Figure S5a with only small variation of 2% between 50 and 100 min as shown in Supporting Information Figure S5a inset. The long-term stability of this photodetector has also been investigated. Six months after we performed measurements shown in Figure 4b,c, we performed similar photocurrent measurement once every day for 15 days, and Supporting Information Figure S5b shows the photocurrent averaged between time = 0 and 200 s upon 254 nm UV illumination. The aligned SnO_2 nanowire photodetector shows good long-term stability with the average photocurrent being 123.05 ± 16.15 nA, which is in the same order of the magnitude as data shown in Figure 4b,c.

Besides working as photodetectors, semiconducting nanowires are also expected to discriminate between different
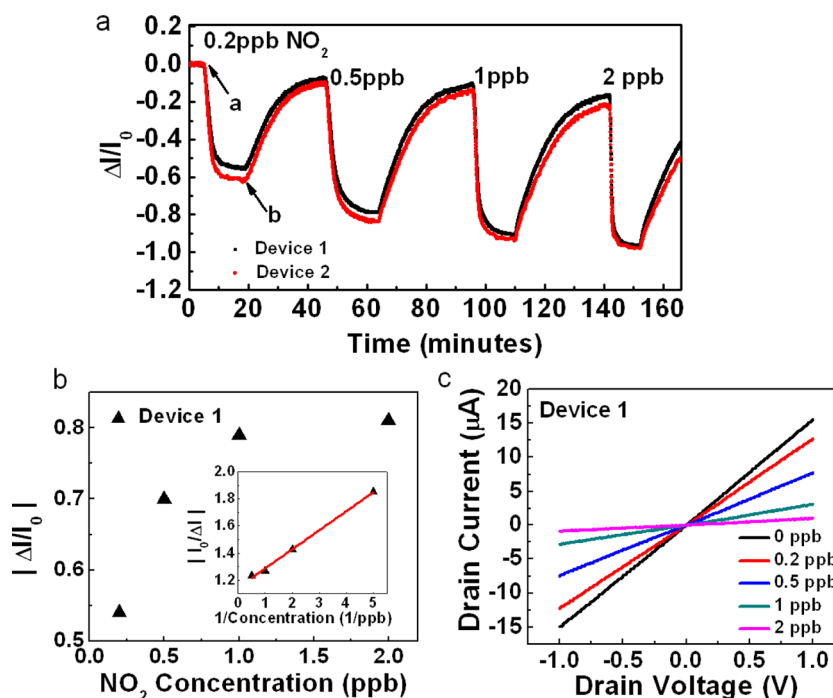
Figure 5. NO$_2$ sensing (a) Real-time detection of NO$_2$ gas of various concentrations by two different aligned SnO$_2$ nanowire devices. NO$_2$ gas is turned on at point "a" and turned off at point "b" (b) Plot of normalized drain current change ($\Delta I/I_0$) against NO$_2$ concentration. In the subplot, the inverse of normalized current and concentration are shown. The black triangles represent measured data, and the red line is a linear fit of the four concentrations data. (b) I_D−V_D plots of device 1 after being introduced to increasing concentrations of NO$_2$.

polarization states of the incident radiation due to their one-dimensional nature.[16,36] SnO$_2$ nanowires possess both an one-dimensional structure and a bandgap in the UV regime and thus are excellent material for polarized UV studies. The polarization detection measurement was carried out by mounting a Glan-laser linear polarizer between the aligned SnO$_2$ nanowire device and the 254 nm wavelength UV lamp. All UV illumination that reached the device was passed through the polarizer as the polarizer was rotated through various angles. Figure 4d shows a plot of the aligned SnO$_2$ nanowire current as a function of the polarizer angle while the voltage between source and drain electrodes of the nanowire device was set at 500 mV. The nanowire conductance showed a periodic dependence (cos 2θ) on the polarization angle (θ) with a period of 180°. From the maximum and minimum conductance values respectively observed under a parallel (G$_\parallel$ = 32 nS) and a perpendicular (G$_\perp$ = 16 nS) field, a polarization ratio of σ = 0.3 was calculated according to σ = (G$_\parallel$ − G$_\perp$)/(G$_\parallel$ + G$_\perp$). This polarization ratio is higher than previously observed values for that of GaN[36] and laser-ablation grown SnO$_2$[16] nanowire devices and equal to the observed value for that of carbon nanotube devices.[38] This improvement further illustrates the significance of controlled orientation of nanostructures for electronic applications.

Metal oxide nanowires have stimulated significant interest for chemical sensing and biosensing applications, which have also been discussed in two recent review papers.[39,40] The mechanisms of conduction changes within SnO$_2$ and other metal oxides due to oxidizing or reducing gas molecules adsorbed on the surface have been well documented.[41−43] The scalability and control allowed by aligned SnO$_2$ nanowires can help to further advance this material as a practical gas sensor. An example of an oxidizing species with strong electron withdrawing capability is the environmental toxin NO$_2$ gas molecule. We chose to detect NO$_2$ to show proof-of-concept

because this gas is a dangerous air pollutant that contributes to the formation of ozone and acid rain. To test the performance of the aligned SnO$_2$ nanowires gas sensors, different concentrations of NO$_2$ are diluted in argon and then introduced to the device surface. Figure 5a shows the real time response to NO$_2$ gas from the aligned SnO$_2$ nanowire sensor device. At time 0, the sensor is illuminated with 254 nm wavelength UV light to increase the device conduction to a suitable level for sensing. Argon is also introduced as the ambient gas. No gate bias was applied to the sensor, and V_D is fixed at 500 mV during the duration of the sensing. At point "a" in the plot, NO$_2$ is introduced to the sensor surface at a concentration of 0.2 ppb. The effect of carrier reduction through the withdrawal of electrons by adsorbed NO$_2$ is seen here. The sensor current immediately decreases about 50−60% and then begins to saturate around point "b", at which point the NO$_2$ gas is turned off while the argon and the UV light are kept on. This procedure is repeated for NO$_2$ at concentrations of 0.5, 1, and 2 ppb. Concentrations beyond 2 ppb saturate the sensor response by turning the sensor to a virtually off state. Our detection limit of 0.2 ppb is comparable to the 0.1 ppb NO$_2$ limit of a functionalized carbon nanotube sensor,[44] which is one of the most sensitive NO$_2$ nanosensors reported to date. This detection limit is more than sufficient for the environmental health standard of 53 ppb. It is also lower than the 2 ppm limit reported from SnO$_2$ nanoribbon sensors[20] and the 0.2 ppm limit from SnO$_2$ nanowire sensors enhanced with additional resistance modulation.[21] Although many other one-dimensional metal oxide NO$_2$ nanosensors have been reported,[21,45−50] their detection limits typically range from 1 ppm (as in the case of CuO nanowire sensors)[49] to 1 ppb (as statistically extrapolated for TiO$_2$ nanowires).[50]

Normalized current change from the real-time sensing is plotted against the NO$_2$ concentration in Figure 5b, where the

first three smaller concentrations are shown to fit the Langmuir-Isotherm model very well, as can be seen from the linear fit in the subplot of inverse responses. The data point for the 2 ppb concentration in the subplot deviates slightly from the linear fit due to the saturation. The 0.2 ppb detection level is confirmed again in a second experiment (Figure 5c) where the aligned SnO_2 nanowire device current is plotted against the drain voltage at each NO_2 concentration. Resistance is shown to decrease significantly as the concentration is increased from 0 to 2 ppb. The clear shift in conduction at all NO_2 concentration levels shows good repeatability and stability of the sensor.

In conclusion, we have demonstrated the growth of parallel, planar SnO_2 nanowires guided by annealed A-plane, annealed M-plane, and R-plane sapphire. A relatively lower synthesis pressure was shown to favor the growth of these guided, planar nanowires while a higher pressure was shown to favor the growth of a nonplanar and unaligned nanowire forest. The alignment orientation of the SnO_2 nanowire and the sapphire substrates were explored using XRD measurements. A straightforward photolithography process was demonstrated for patterning the aligned nanowires for working FETs with high mobilities and on/off ratios sufficient for driving an external OLED with a clear distinction between on and off intensities. The electrical parameters support the advantages of aligned SnO_2 nanowire transistors over network SnO_2 nanowire FETs. This is further demonstrated in the performance of the aligned SnO_2 nanowire FET for polarized UV light detection, where the polarization ratio is higher than that from laser-ablation synthesized nanowire FETs. And finally, we demonstrated that the SnO_2 nanowire FET can be used as NO_2 detectors with sensitivity below the ppb range. As SnO_2 has been an important material for many of the applications investigated in this paper, this demonstration of aligned SnO_2 nanowires is an important step toward a more scalable and higher-performance SnO_2 nanowire devices. Having established this initial platform, we will further investigate the synthesis and fabrication process to achieve FETs with low device-to-device variations for future applications such as transparent and flexible electronics and sensors.

ASSOCIATED CONTENT

Ⓢ Supporting Information

Materials and methods used for aligned SnO_2 nanowires synthesis and device fabrication. Histograms of nanowire density, defect density, and misalignment angle of nanowires grown on annealed A-plane, annealed M-plane, and R-plane sapphire substrates. Schematic of FIB preparation of nanowire cross-section, TEM images of the cross-section, and electron diffraction pattern with simulated diffraction patterns. High-resolution TEM image of the cross section of an aligned SnO_2 nanowire on an R-plane sapphire substrate. High-resolution SEM image of an aligned SnO_2 nanowire on R-plane sapphire. SEM image of nonaligned SnO_2 nanowires on R-plane sapphire synthesized at atmospheric pressure. Histograms of electrical performance: on-state current, on/off ratio, transconductance, and electron mobilities from 20 devices. Photocurrent stability measurements. This material is available free of charge via the Internet at http://pubs.acs.org.

AUTHOR INFORMATION

Corresponding Author
*E-mail: chongwuz@usc.edu.

Author Contributions
‖X.W. and N.A contributed equally.

Notes
The authors declare no competing financial interest.

REFERENCES

(1) Jin, S.; Whang, D.; McAlpine, M. C.; Friedman, R. S.; Wu, Y.; Lieber, C. M. *Nano Lett.* **2004**, *4* (5), 915−919.

(2) Whang, D.; Jin, S.; Wu, Y.; Lieber, C. M. *Nano Lett.* **2003**, *3* (9), 1255−1259.

(3) Kim, F.; Kwan, S.; Akana, J.; Yang, P. *J. Am. Chem. Soc.* **2001**, *123* (18), 4360−1.

(4) Melosh, N. A.; Boukai, A.; Diana, F.; Gerardot, B.; Badolato, A.; Petroff, P. M.; Heath, J. R. *Science (New York, N.Y.)* **2003**, *300* (5616), 112−5.

(5) Yu, G.; Cao, A.; Lieber, C. M. *Nat. Nanotechnol.* **2007**, *2* (6), 372−7.

(6) Huang, Y.; Duan, X.; Wei, Q.; Lieber, C. M. *Science (New York, N.Y.)* **2001**, *291* (5504), 630−3.

(7) Smith, P. A.; Nordquist, C. D.; Jackson, T. N.; Mayer, T. S.; Martin, B. R.; Mbindyo, J.; Mallouk, T. E. *Appl. Phys. Lett.* **2000**, *77* (9), 1399−1401.

(8) Yao, J.; Yan, H.; Lieber, C. M. *Nat. Nanotechnol.* **2013**, *8* (5), 329−335.

(9) Tsivion, D.; Schvartzman, M.; Popovitz-Biro, R.; von Huth, P.; Joselevich, E. *Science (New York, N.Y.)* **2011**, *333* (6045), 1003−7.

(10) Nikoobakht, B.; Michaels, C. A.; Stranick, S. J.; Vaudin, M. D. *Appl. Phys. Lett.* **2004**, *85* (15), 3244−3246.

(11) Tsivion, D.; Schvartzman, M.; Popovitz-Biro, R.; Joselevich, E. *ACS Nano* **2012**, *6* (7), 6433−45.

(12) Zi, Y.; Jung, K.; Zakharov, D.; Yang, C. *Nano Lett.* **2013**, *13* (6), 2786−2791.

(13) Mattila, M.; Hakkarainen, T.; Jiang, H.; Kauppinen, E. I.; Lipsanen, H. *Nanotechnology* **2007**, *18*, 155301.

(14) Camagni, P.; Faglia, G.; Galinetto, P.; Perego, C.; Samoggia, G.; Sberveglieri, G. *Sens. Actuators, B* **1996**, *31* (1−2), 99−103.

(15) Dattoli, E. N.; Wan, Q.; Guo, W.; Chen, Y.; Pan, X.; Lu, W. *Nano Lett.* **2007**, *7* (8), 2463−9.

(16) Liu, Z. Q.; Zhang, D. H.; Han, S.; Li, C.; Tang, T.; Jin, W.; Liu, X. L.; Lei, B.; Zhou, C. W. *Adv. Mater.* **2003**, *15* (20), 1754−+.

(17) Amin, N.; Isaka, T.; Yamada, A.; Konagai, M. *Sol. Energy Mater. Sol. Cells* **2001**, *67* (1−4), 195−201.

(18) Comini, E.; Faglia, G.; Sberveglieri, G. *Sens. Actuators, B* **2001**, *78* (1−3), 73−77.

(19) Maiti, A.; Rodriguez, J. A.; Law, M.; Kung, P.; McKinney, J. R.; Yang, P. D. *Nano Lett.* **2003**, *3* (8), 1025−1028.

(20) Law, M.; Kind, H.; Messer, B.; Kim, F.; Yang, P. D. *Angew. Chem., Int. Ed.* **2002**, *41* (13), 2405−2408.

(21) Choi, Y. J.; Hwang, I. S.; Park, J. G.; Choi, K. J.; Park, J. H.; Lee, J. H. *Nanotechnology* **2008**, *19*, 095508.

(22) Ago, H.; Nakamura, K.; Ikeda, K.; Uehara, N.; Ishigami, N.; Tsuji, M. *Chem. Phys. Lett.* **2005**, *408* (4−6), 433−438.

(23) Ryu, K.; Badmaev, A.; Wang, C.; Lin, A.; Patil, N.; Gomez, L.; Kumar, A.; Mitra, S.; Wong, H. S. P.; Zhou, C. W. *Nano Lett.* **2009**, *9* (1), 189−197.

(24) Leonardy, A.; Hung, W.-Z.; Tsai, D.-S.; Chou, C.-C.; Huang, Y.-S. *Cryst. Growth Des.* **2009**, *9* (9), 3958−3963.

(25) Semancik, S.; Cavicchi, R. E. *Thin Solid Films* **1991**, *206* (1−2), 81−87.

(26) Dominguez, J. E.; Pan, X. Q.; Fu, L.; Van Rompay, P. A.; Zhang, Z.; Nees, J. A.; Pronko, P. P. *J. Appl. Phys.* **2002**, *91* (3), 1060−1065.

(27) Lei, B.; Li, C.; Zhang, D.; Zhou, Q. F.; Shung, K. K.; Zhou, C. *Appl. Phys. Lett.* **2004**, *84* (22), 4553−4555.

(28) Ishikawa, F. N.; Chang, H.-K.; Curreli, M.; Liao, H.-I.; Olson, C. A.; Chen, P.-C.; Zhang, R.; Roberts, R. W.; Sun, R.; Cote, R. J.; Thompson, M. E.; Zhou, C. *ACS Nano* **2009**, *3* (5), 1219−1224.

(29) Kolmakov, A.; Zhang, Y.; Cheng, G.; Moskovits, M. *Adv. Mater.* **2003**, *15* (12), 997−1000.

(30) Kordos, P.; Gregusova, D.; Stoklas, R.; Cico, K.; Novak, J. *Appl. Phys. Lett.* **2007**, *90* (12), 123513.

(31) Martel, R.; Schmidt, T.; Shea, H. R.; Hertel, T.; Avouris, P. *Appl. Phys. Lett.* **1998**, *73* (17), 2447−2449.

(32) Zhou, C. W.; Kong, J.; Yenilmez, E.; Dai, H. J. *Science (New York, N.Y.)* **2000**, *290* (5496), 1552−1555.

(33) Huh, J.; Joo, M. K.; Jang, D.; Lee, J. H.; Kim, G. T. *J. Mater. Chem.* **2012**, *22* (45), 24012−24016.

(34) Forrest, S. R.; Burrows, P. E.; Thompson, M. E. *Laser Focus World* **1995**, *31* (2), 99−&.

(35) Sheats, J. R.; Antoniadis, H.; Hueschen, M.; Leonard, W.; Miller, J.; Moon, R.; Roitman, D.; Stocking, A. *Science (New York, N.Y.)* **1996**, *273* (5277), 884−888.

(36) Han, S.; Jin, W.; Zhang, D. H.; Tang, T.; Li, C.; Liu, X. L.; Liu, Z. Q.; Lei, B.; Zhou, C. W. *Chem. Phys. Lett.* **2004**, *389* (1−3), 176−180.

(37) Zhang, D.; Li, C.; Han, S.; Liu, X.; Tang, T.; Jin, W.; Zhou, C. *Appl. Phys. A: Mater. Sci. Process.* **2003**, *77* (1), 163−166.

(38) Freitag, M.; Martin, Y.; Misewich, J. A.; Martel, R.; Avouris, P. H. *Nano Lett.* **2003**, *3* (8), 1067−1071.

(39) Po-Chiang, C.; Guozhen, S.; Chongwu, Z. *IEEE Trans. Nanotechnol.* **2008**, *7* (6), 668−682.

(40) Curreli, M.; Rui, Z.; Ishikawa, F. N.; Chang, H.-K.; Cote, R. J.; Chongwu, Z.; Thompson, M. E. *IEEE Trans. Nanotechnol.* **2008**, *7* (6), 651−667.

(41) Kolmakov, A.; Klenov, D. O.; Lilach, Y.; Stemmer, S.; Moskovits, M. *Nano Lett.* **2005**, *5* (4), 667−673.

(42) Fryberger, T. B.; Semancik, S. *Sens. Actuators, B* **1990**, *2* (4), 305−309.

(43) Li, C.; Lei, B.; Zhang, D.; Liu, X.; Han, S.; Tang, T.; Rouhanizadeh, M.; Hsiai, T.; Zhou, C. *Appl. Phys. Lett.* **2003**, *83* (19), 4014−4016.

(44) Pengfei, Q. F.; Vermesh, O.; Grecu, M.; Javey, A.; Wang, O.; Dai, H. J.; Peng, S.; Cho, K. J. *Nano Lett.* **2003**, *3* (3), 347−351.

(45) Cao, B. B.; Chen, J. J.; Tang, X. J.; Zhou, W. L. *J. Mater. Chem.* **2009**, *19* (16), 2323−2327.

(46) Rout, C. S.; Ganesh, K.; Govindaraj, A.; Rao, C. N. R. *Appl. Phys. A: Mater. Sci. Process.* **2006**, *85* (3), 241−246.

(47) Zhang, D. H.; Liu, Z. Q.; Li, C.; Tang, T.; Liu, X. L.; Han, S.; Lei, B.; Zhou, C. W. *Nano Lett.* **2004**, *4* (10), 1919−1924.

(48) Ahn, M. W.; Park, K. S.; Heo, J. H.; Kim, D. W.; Choi, K. J.; Park, J. G. S*Sens. Actuators, B* **2009**, *138* (1), 168−173.

(49) Kim, Y. S.; Hwang, I. S.; Kim, S. J.; Lee, C. Y.; Lee, J. H. *Sens. Actuators, B* **2008**, *135* (1), 298−303.

(50) Kim, I. D.; Rothschild, A.; Lee, B. H.; Kim, D. Y.; Jo, S. M.; Tuller, H. L. *Nano Lett.* **2006**, *6* (9), 2009−2013.